JGR Space Physics

RESEARCH ARTICLE
10.1029/2025JA034770

Special Collection:
Solar Wind: Origin, Acceleration, and Outflow

Kinetic-Based Macro-Modeling of the Solar Wind at Large Heliocentric Distances: Kappa Electrons at the Exobase

A. Vinogradov[1], M. Lazar[1,2], I. Zouganelis[3], V. Pierrard[4,5], and S. Poedts[1,6]

[1]Centre for Mathematical Plasma-Astrophysics, KU Leuven, Leuven, Belgium, [2]Theoretical Physics IV, Faculty for Physics and Astronomy, Ruhr-University Bochum, Bochum, Germany, [3]European Space Agency (ESA), European Space Astronomy Centre (ESAC), Madrid, Spain, [4]Royal Belgian Institute for Space Aeronomy (BIRA-IASB), Space Physics, Solar Terrestrial Center of Excellence (STCE), Brussels, Belgium, [5]Earth and Life Institute-Climate Sciences (ELI-C), Université Catholique de Louvain, Louvain-la-Neuve, Belgium, [6]Institute of Physics, University of Maria Curie-Skłodowska, Lublin, Poland

Abstract Recent evidence from Parker Solar Probe on the suprathermal electrons with Kappa-type velocity distributions in the outer corona has revived interest in the kinetic-based macro-modeling of the solar (SW), aiming to explain its properties. Invoked in kinetic modeling of nonequilibrium plasmas, standard Kappa distributions (SKDs) have been adjusted to the regularized Kappa distributions (RKDs) to fix the inconsistencies of SKD and develop consistent fluid modeling of space plasmas. We propose a new analysis of these properties at large heliocentric distances based on the existence of RKD electrons at the exobase. This new semi-analytic formalism is inspired by the methodology proposed initially by Meyer-Vernet and Issautier (1998), https://doi.org/10.1029/98ja02853. Compared to SKDs, the results for RKDs have extended applicability, since all moments can be defined and calculated consistently for all values of the κ parameter, even lower than the critical ones (e.g., $\kappa_c = 3/2$ imposed to the second-order moment) of SKDs. However, the excess energy of the more energetic suprathermal electrons associated with low values of $\kappa \lesssim 3/2$, is regulated by the RKD-specific cutoff parameter $\alpha < 1$. The estimates for, for example, the temperature and bulk velocity of the SW, remain at realistic values even for small $3/2 < \kappa \lesssim 2$, which would otherwise exceed specific observations. One can thus model a higher abundance of suprathermal electrons at the exobase (e.g., $\kappa \leqslant 3/2$), which is plausible for the sources of energetic events (flares and coronal mass ejections), and also in the astrospheres of stars with coronas hotter than the Sun's.

Plain Language Summary The solar wind is a flow of charged particles, electrons and ions/protons, emerging from the outer solar corona and reaching speeds between 300 and 800 km/s in interplanetary space. Kinetic-exospheric models show that the solar wind can be driven by light but energetic, suprathermal electrons that escape solar gravity and create an electric field that pulls protons away from the Sun. We provide an improved semi-analytic model of the long-distance solar wind ($r > 0.3$ AU) that uses a regularized Kappa distribution to realistically capture the effects of suprathermal electrons at the exobase of a few solar radii. This distribution resolves the inconsistencies and limitations of standard Kappa distributions, offering a consistent extension of such macro-models, even in the presence of enhanced suprathermal electrons at the exobase, characteristic of more energetic coronal outflows.

Key Points:

- Suprathermal electrons with Kappa distributions (KDs) in the solar corona play a key role in the formation/acceleration of the solar wind
- A semi-analytic kinetic model is built for the large-distance solar wind by assuming electrons with regularized KDs (RKDs) at the exobase
- RKDs resolve the existing inconsistencies and reduce possible overestimations from the increased presence of suprathermal electrons

Correspondence to:
A. Vinogradov,
alexander.vinogradov@kuleuven.be

Citation:
Vinogradov, A., Lazar, M., Zouganelis, I., Pierrard, V., & Poedts, S. (2026). Kinetic-based macro-modeling of the solar wind at large heliocentric distances: Kappa electrons at the exobase. *Journal of Geophysical Research: Space Physics*, *131*, e2025JA034770. https://doi.org/10.1029/2025JA034770

Received 16 OCT 2025
Accepted 4 FEB 2026

Author Contributions:
Conceptualization: M. Lazar
Formal analysis: A. Vinogradov, M. Lazar, S. Poedts
Funding acquisition: M. Lazar, S. Poedts
Investigation: A. Vinogradov, M. Lazar
Methodology: A. Vinogradov, M. Lazar, V. Pierrard
Project administration: M. Lazar, S. Poedts
Resources: M. Lazar, S. Poedts
Software: A. Vinogradov
Supervision: M. Lazar
Validation: A. Vinogradov, V. Pierrard
Visualization: A. Vinogradov, M. Lazar
Writing – original draft: A. Vinogradov, M. Lazar, S. Poedts
Writing – review & editing: A. Vinogradov, M. Lazar, S. Poedts

© 2026. American Geophysical Union. All Rights Reserved.

1. Introduction

The ability of kinetic exospheric models to produce realistic estimates of the solar wind (SW) properties depends on how good the assumptions made for the initial or boundary conditions are, especially those at the exobase (a few solar radii), the altitude above which there are no collisions (Lamy et al., 2003; Lemaire & Scherer, 1971; Maksimovic, Pierrard, & Lemaire, 1997; Péters de Bonhome et al., 2025; Pierrard et al., 2001, 2011; Vocks et al., 2005; Zouganelis et al., 2004). While these estimates have been able to be evaluated for decades by comparing them with the SW properties measured since the first space missions at different heliocentric distances (such as Helios, Ulysses and those orbiting Earth), the scenarios proposed for the exobase are only now being confirmed (or not) thanks to coronal observations by the Parker Solar Probe [PSP] (Abraham et al., 2022; Zheng et al., 2024).

A key ingredient in the formation and acceleration of the SW is energetic suprathermal electrons, which are not in thermal equilibrium and can be described by Kappa (κ-)power-law velocity distributions (In Lazar &

Fichtner, 2021; Pierrard & Lazar, 2010). Kappa electrons are ubiquitous in the SW (Maksimovic, Pierrard, & Riley, 1997; Wilson et al., 2019; Štverák et al., 2008), and PSP data also support their presence in the outer corona (Abraham et al., 2022; Zheng et al., 2024). Suprathermal electrons enhance the number of electrons escaping at the exobase and implicitly determine an increase in the ambipolar electrostatic (ES) potential that drags protons (overcoming gravitational attraction) and accelerates them to supersonic speeds (Lamy et al., 2003; Zouganelis et al., 2004). Moreover, lower exobases lead to increased bulk velocities of the SW (Zouganelis et al., 2004), in agreement with the (hypothetical) subcoronal origin of fast outflows, commonly linked to coronal holes. Thus, exospheric models consider the exobase at small distances, below 10 R_S, assuming that beyond the exobase particle-particle collisions are no longer effective in establishing thermodynamic equilibrium (Lamy et al., 2003; Meyer-Vernet & Issautier, 1998; Zouganelis et al., 2004). Recent in situ observations of PSP down to 10 R_S support these scenarios by revealing electrons with Kappa (non-Maxwellian) VDs, with κ reaching low values around 4, and even lower, as suggested by the decreasing radial trend (Abraham et al., 2022; Zheng et al., 2024). There are also indirect indications from modeling supporting the presence of such energetic electron populations in the solar corona, whose inclusion enhances both heavy ion charge states and solar wind acceleration, improving agreement with observations (Lomazzi et al., 2025; Shen et al., 2025). An exobase at low radial distance like $6R_S$ (Lemaire & Scherer, 1971; Meyer-Vernet & Issautier, 1998) can be justified not only by the collisional rate, but also the configuration of the magnetic field opening to the interplanetary space at this distance, which can explain why the slow wind is characterized by a higher exobase than the fast wind (Pierrard et al., 2023).

The values of the parameter κ measured for the electron velocity distributions (VDs hereafter) in high-speed SW are lower (the suprathermal tails are stronger) than in slow winds (Lazar, Pierrard, et al., 2020; Maksimovic, Pierrard, & Riley, 1997), also suggesting a relationship between the suprathermal electrons and the bulk speed. The self-consistent evaluation of the ES potential at each position in space is not straightforward, being generally achieved by iterative calculations based on the neutrality of the electric charge and current, sufficiently well preserved in the SW (Feldman et al., 1975). An analytical or semi-analytical solution of this ES potential is thus of great interest, as it can significantly facilitate calculation even in numerical codes of exospheric models (Meyer-Vernet & Issautier, 1998; Osuna Alcalaya et al., 2021).

Despite the progress in describing the VDs observed in non-equilibrium plasmas in space, standard Kappa distributions (SKDs) still have inconsistencies that have been resolved more recently by the so-called regularized Kappa distributions (RKDs) (In Lazar & Fichtner, 2021; Scherer et al., 2017). The additional exponential factor introduces the new cutoff parameter $0 < \alpha < 1$, which primarily reduces the unrealistic contribution of superluminal (nonphysical) particles with velocities $v > c$ (where c is the speed of light in vacuum). Furthermore, important for large-scale (macro) models, such as those pursued by exospheric kinetic modeling, is that all moments of RKDs are well defined for all values of the parameter $\kappa > 0$. For SKDs, moments of order $l \geqslant 2$ and the corresponding transport coefficients take finite values only for large enough $\kappa > (l + 1)/2$, which is not the case for RKDs (Husidic et al., 2022; Lazar, Scherer, et al., 2020). The capabilities to describe suprathermal populations and their implications are consistently expanded. Numerical solutions of a preliminary model constructed for RKD electrons at the exobase have been reported, limiting, however, to large values of $\kappa > (l + 1)/2$ for easier comparison with previous results obtained for SKD electrons (Pierrard et al., 2023). Therefore, RKDs also offer an improved alternative for describing VDs observed in situ, without having to disregard those with strong suprathermal tails, associated with a reduced parameter κ (Scherer et al., 2021).

This paper proposes a new kinetic modeling of SW properties at large heliocentric distances from the exobase, following the semi-analytic formalism of Meyer-Vernet and Issautier (1998). These properties depend on the nature of the VDs of the electron and proton populations at the exobase. This already follows from the general expressions for the SW parameters, derived previously (for arbitrary VDs) at large distances, and briefly reviewed in Section 2. Even at large heliocentric distances, up to 1 AU and beyond, where the variation with distance remains roughly constant, the absolute values of the SW parameters may significantly depend on the nature of the electron VDs at the exobase (Meyer-Vernet & Issautier, 1998). To be sufficiently explicit, Section 3 presents a retrospective of the previous approach based on the presence of SKD electrons at the exobase, as well as a new extended analysis that provides analytic solutions that accurately reproduce the exact ones. The new semi-analytic model, assuming RKD electrons at the exobase, is provided in Section 4. The complexity of the solutions obtained in this case for the ES potential and the SW parameters, expressed in terms of hypergeometric Tricomi functions, precludes rigorous approximations and simplified, fully analytical forms. However, kinetic models based on RKD electrons offer opportunities to analyze new conditions at the exobase, with suprathermal electrons of increased

densities and energies that SKDs cannot describe. These could thus explain the coronal outflows with bulk velocities much higher than those of the SW associated with energetic solar events, but can also contribute to modeling the atmospheres and winds of stars with coronas hotter than the Sun. Such perspectives are discussed, along with the results of this work, in Section 5.

2. General Approach

Following the general formalism in Meyer-Vernet and Issautier (1998), we present here only the main relationships and parameters used to determine the ES potential at the exobase, the terminal SW speed, and the heliocentric radial profiles at large distances. At this stage, these are independent of any specific form of electron or proton VDs, but will be specialized to SKD electrons in Section 3 and to RKD electrons in Section 4. General expressions of the moments for the (arbitrary) distribution functions of protons and electrons are presented in Appendix A and B, respectively. For additional details that may aid in understanding these results, we recommend consulting the basic formalism in Meyer-Vernet and Issautier (1998).

2.1. Boundary Conditions at the Exobase

To evaluate the ES potential at the exobase level, we enforce the condition of zero net flux of charge, which is given by the equality of electron (subscript e) and proton (subscript p) fluxes (Meyer-Vernet & Issautier, 1998)

$$F_e \equiv \int_{V_0}^{\infty} dv v^3 f_{e0}(v) = F_p \equiv \int_0^{\infty} dv v^3 f_{p0}(v), \tag{1}$$

where f_{e0} and f_{p0} are electron and proton distribution functions at the exobase level $r = r_0$. The parameter V_0, introduced in Meyer-Vernet and Issautier (1998), corresponds to the characteristic electron escape speed; only electrons with $v > V_0$ contribute to the escaping flux. It is related to the ES potential $\Phi_E(r_0)$ through Equation 9 in Meyer-Vernet and Issautier (1998),

$$V_0 = \sqrt{\frac{2e\Phi_E(r_0)}{m_e}}. \tag{2}$$

The distribution functions $f_{p0}(v)$ and $f_{e0}(v)$ are normalized according to Equations 18 and 19 of Meyer-Vernet and Issautier (1998).

$$n_e(r_0) = 4\pi \int_0^{\infty} dv\ v^2 f_{e0}(v) - 2\pi \int_{V_0}^{\infty} dv\ v^2 f_{e0}(v), \tag{3}$$

$$n_p(r_0) = 2\pi \int_0^{\infty} dv\ v^2 f_{p0}(v). \tag{4}$$

Once normalizations are determined, we substitute $f_{p0}(v)$ and $f_{e0}(v)$ into Equation 1, use the quasi-neutrality condition $n_e(r_0) = n_p(r_0)$, and solve Equation 1 for $\Phi_E(r_0)$. This boundary value of the potential allows us to estimate the terminal SW speed V_{SW} from the approximate proton energy balance $m_p V_{SW}^2/2 \approx e\Phi_E(r_0) - m_p\Phi_G(r_0)$ (Meyer-Vernet & Issautier, 1998), as

$$V_{SW} \approx \{2[e\Phi_E(r_0) - m_p\Phi_G(r_0)]/m_p\}^{1/2}, \tag{5}$$

with the gravitational potential at the exobase given by

$$\Phi_G(r_0) = \frac{GM_S}{r_0}. \tag{6}$$

2.2. Radial Profiles at Large Distances

We adopt the asymptotic expressions for radial profiles derived by Meyer-Vernet and Issautier (1998). These expressions are valid in the limit of large distances, where $\eta(r) = (r_0/r)^2 \ll 1$. The radial profile of the density is given by

$$n_p(r) = C_0\eta(r) = C_0\left(\frac{r_0}{r}\right)^2, \tag{7}$$

where

$$C_0 = \pi\int_0^\infty dv \frac{v^3}{\sqrt{(v^2 + V_{p0}^2)}} f_{p0}(v), \tag{8}$$

and

$$V_{p0} = \sqrt{\frac{2}{m_p}(e\Phi_E(r_0) - \Phi_G(r_0))}. \tag{9}$$

The radial profile of the ES potential is given by

$$\Phi_E(r) = \frac{m_e}{2e}\left(\frac{C_0}{D_0}\right)^{2/3}\eta^{2/3} = \frac{m_e}{2e}\left(\frac{C_0}{D_0}\right)^{2/3}(r_0/r)^{4/3}, \tag{10}$$

where

$$D_0 = \frac{4\pi}{3}f_{e0}(V_0), \tag{11}$$

depends on the electron VD. The electron temperature can be expressed as a sum of two terms

$$T_e(r) = T_{4/3}(r) + T_C. \tag{12}$$

The first term corresponds to the effect of nonescaping electrons and depends explicitly on r

$$T_{4/3}(r) = \frac{m_e}{5k_B}\left(\frac{C_0}{D_0}\right)^{2/3}\eta^{2/3} \propto \left(\frac{r_0}{r}\right)^{4/3}. \tag{13}$$

The second term, T_C, arises from escaping electrons. It is independent of the radial distance r and is given by

$$T_C = \frac{m_e\, B_2}{3k_B C_0}, \tag{14}$$

where

$$B_2 = \pi\int_{V_0}^\infty dv v^3\sqrt{v^2 - V_0^2} f_{e0}(v). \tag{15}$$

These relations are the general framework of our study. In the following sections, we apply this procedure to specific cases: SKD electrons with Maxwellian protons (Section 3), and then RKD electrons (Section 4).

3. SKD Electrons and Maxwellian Protons at the Exobase

The proton VD at the exobase is assumed to be Maxwellian:

$$f_{0p} = A_p \exp\left(\frac{v^2}{w_{p0}^2}\right), \tag{16}$$

and the normalization constant A_p is derived from Equation 4

$$A_p = \frac{2n_p(r_0)}{(\pi w_{p0}^2)^{3/2}}. \tag{17}$$

In the previous approach, VD models were introduced with normalization constants, such as generic densities, for example, n_{p0} for protons and n_{e0} for electrons (Meyer-Vernet & Issautier, 1998). Here we show that (non-normalized) physical quantities at the exobase can also be used, such as for the densities $n_p(r_0)$ and $n_e(r_0)$, as well as thermal velocities w_{p0} and w_{e0}. We first revisit the approach in Meyer-Vernet and Issautier (1998), where the electrons follow an SKD

$$f_{0e} = A_e\left(1 + \frac{v^2}{\kappa w_{e0}^2}\right)^{-\kappa-1}. \tag{18}$$

The expression in Equation 3 is then used to find the normalization constant

$$A_e = \frac{n_e(r_0)}{(\pi\kappa w_{e0}^2)^{3/2}} \frac{1}{\left[\frac{1}{2}\frac{\Gamma(\kappa-1/2)}{\Gamma(\kappa+1)} + \frac{B_{x_0}(3/2,\kappa-1/2)}{\sqrt{\pi}}\right]}, \tag{19}$$

where

$$B_{x_0}(a,b) = \int_0^{x_0} t^{a-1}(1-t)^{b-1}dt, \tag{20}$$

is the incomplete beta function with

$$x_0 = \frac{V_0^2}{\kappa w_{e0}^2 + V_0^2} = \frac{y}{y+1} < 1, \tag{21}$$

and the key parameter

$$y = \frac{V_0^2}{\kappa w_{e0}^2}. \tag{22}$$

The equivalence between our normalization for the Kappa distribution and that in Meyer-Vernet and Issautier (1998) is proven in Appendix C. The ES potential at the exobase $\Phi_E(r_0)$ is then derived, according to its definition, from Equation 22

$$\Phi_E(r_0) \equiv \frac{m_e V_0^2}{2e} = \frac{m_e \kappa w_{e0}^2}{2e} y. \tag{23}$$

3.1. Exact (Numerical) Solutions

Using Equations 16–19 and charge neutrality at r_0, $n_e(r_0) = n_p(r_0)$, the zero-net current condition in Equation 1 gives us

Table 1
Values Obtained for the Exact Solutions of y, $\Phi_E(r_0)$, and V_{SW} for $w_{p0} = 182$ km/s ($T_{p0} = 2 \times 10^6$ K) and $w_{e0} = 5.5 \times 10^3$ km/s ($T_{e0} = 10^6$ K), and Different Values of κ

κ	y	$\Phi_E(r_0)$ (V)	V_{SW} (km/s)
1.6	2011.4	2.77×10^5	7,285
2	95.3	1.642×10^4	1,756
3	9.5	2.468×10^3	640
5	2.4	1.036×10^3	367
10	0.8	6.515×10^2	247
20	0.3	5.375×10^2	198

$$\frac{w_{p0}}{w_{e0}} = \frac{1+\kappa y}{\sqrt{\kappa}(\kappa-1)} \frac{(1+y)^{-\kappa}}{\frac{1}{2}\frac{\Gamma(\kappa-1/2)}{\Gamma(\kappa+1)} + \frac{B_{x_0}(3/2,\kappa-1/2)}{\sqrt{\pi}}}. \tag{24}$$

We numerically solve Equation 24 for y, using the Brent root-finding method (Brent, 1973). Once y is computed, we then derive the ES potential at the exobase $\Phi_E(r_0)$ and the terminal SW speed $V_{\rm SW}$, using Equations 5 and 23 respectively. We assume $r_0 = 6R_S$, as in Lemaire and Scherer (1971) and Meyer-Vernet and Issautier (1998), where R_S is the solar radius. This is used to evaluate the gravitational potential defined in Equation 6, which then enters into Equation 5.

Table 1 shows the exact numerical solutions y for a range of κ values, together with the parameters $\Phi_E(r_0)$ and V_{SW} derived as described above. Calculations are performed for standard coronal values at the exobase, namely, for a proton thermal speed $w_{p0} = 182$ km/s, corresponding to $T_{p0} = m_p w_{p0}^2/2k_B = 2 \times 10^6$ K, and an electron thermal speed $w_{e0} = 5.5 \times 10^3$ km/s, corresponding to $T_{e0} = m_e w_{e0}^2/2k_B = 10^6$ K (Meyer-Vernet & Issautier, 1998). These are typical values of proton and electron temperatures in the corona, in this case associated with the exobase at $r_0 = 6R_S$. According to Table 1, the ES potential $\Phi_E(r_0)$ is lower for larger κ, while the SW is slower. This is a well-known effect (Maksimovic, Pierrard, & Lemaire, 1997) because a larger κ means the electron distribution is closer to a Maxwellian, with a weaker high-energy tail. Fewer escaping electrons require a smaller confining potential, which in turn provides less acceleration for the SW.

3.2. Analytical Approximations

As argued in Meyer-Vernet and Issautier (1998), V_0 is generally much larger than the most probable speed of the electron distribution $f_{e0}(v)$, such that $V_0 \gg w_{e0}$, while the contribution of the second term in Equation 3 is therefore negligible. In this limit, if κ is small enough, we can assume $y = V_0^2/(\kappa w_{e0}^2) \gg 1$, and find $x_0 \to 1$, while our $B_{x_0}(3/2, \kappa - 1/2)$ reduces to a constant

$$\lim_{x_0 \to 1} B_{x_0}(3/2, \kappa - 1/2) = \frac{\sqrt{\pi}}{2} \frac{\Gamma(\kappa - 1/2)}{\Gamma(\kappa+1)}. \tag{25}$$

Using (Equations 24 and 25) reduces to

$$\frac{w_{p0}}{w_{e0}} = \frac{(1+\kappa y)(1+y)^{-\kappa}}{\sqrt{\kappa}(\kappa-1)} \frac{\Gamma(\kappa+1)}{\Gamma(\kappa-1/2)}, \tag{26}$$

which can restrain to

$$\kappa y + 1 = a(y+1)^{\kappa}, \tag{27}$$

with

$$a = \frac{w_{p0}}{w_{e0}} \frac{\Gamma(\kappa-1/2)}{\sqrt{\kappa}\Gamma(\kappa-1)}. \tag{28}$$

In the same limit of large $y_0 \gg 1$, also invoked in Meyer-Vernet and Issautier (1998), we obtain an analytical zero-order approximation,

$$y_0 \simeq (\kappa/a)^{1/(\kappa-1)}, \tag{29}$$

and the corresponding expression of the ES potential follows from Equation 23

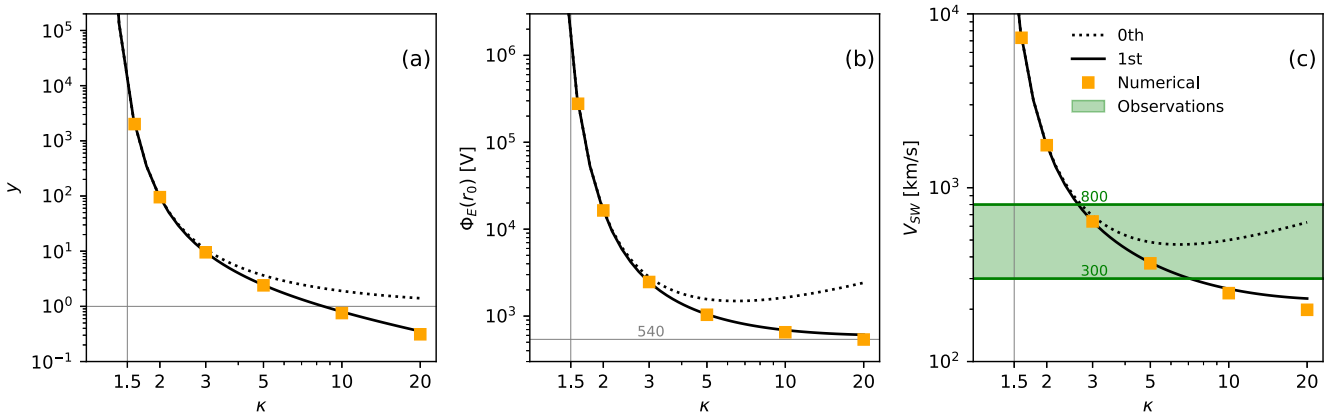

Figure 1. Dependence of the solutions at the exobase on κ for SKD electrons: (a) parameter y; (b) ES potential (dashed line marks the Maxwellian limit, $\kappa \to \infty$, when $\Phi_E(r_0) \simeq 540$ V); (c) asymptotic (terminal) SW speed $V_{\rm SW}$. Plotted are the zero-order approximations (dotted lines), the first-order approximations (solid lines), and the exact numerical results (orange squares). The greenish range in panel (c) delimits the observed limits of the SW speed (300–800 km/s).

$$\Phi_E(r_0) = \frac{m_e w_{e0}^2}{2e}\left(\frac{\kappa^\kappa}{a}\right)^{\frac{1}{\kappa-1}}. \tag{30}$$

This result was first obtained in Meyer-Vernet and Issautier (1998) in their Equation 73, taking into account their definition Equation 58. However, the zero-order approximation is not accurate for large κ, as shown here in Figure 1. Therefore, in the following, we derive a first-order approximation, which extends the validity of the analytic solution for larger κ. We introduce the correction term δy, such that

$$y \simeq y_0 + \delta y. \tag{31}$$

Substituting Equation 31 into Equation 27 gives

$$1 + \kappa(y_0 + \delta y) = a(1 + y_0 + \delta y)^\kappa, \tag{32}$$

which can be rewritten as

$$1 + \kappa(y_0 + \delta y) = a y_0^\kappa \left(1 + \frac{1 + \delta y}{y_0}\right)^\kappa. \tag{33}$$

For large y_0, we assume that the correction δy is small, that is, $(1 + \delta y)/y_0 \ll 1$. Expanding to first order gives

$$\left(1 + \frac{1 + \delta y}{y_0}\right)^\kappa \approx 1 + \frac{\kappa(1 + \delta y)}{y_0}. \tag{34}$$

Substituting this expansion into Equation 33 yields

$$1 + \kappa(y_0 + \delta y) = a y_0^\kappa \left[1 + \frac{\kappa(1 + \delta y)}{y_0}\right]. \tag{35}$$

From Equation 22, we have $y_0^{\kappa-1} = \kappa/a$, and multiplying both sides by $a y_0$ gives $a y_0^\kappa = \kappa y_0$, which is then substituted in Equation 35 to find

$$1 + \kappa(y_0 + \delta y) = \kappa y_0 \left(1 + \frac{\kappa(1 + \delta y)}{y_0}\right), \tag{36}$$

which simplifies,

$$1 + \kappa\delta y = \kappa^2(1 + \delta y), \tag{37}$$

to finally obtain

$$\delta y = -\frac{\kappa + 1}{\kappa}. \tag{38}$$

Substituting Equations 29 and 38 into Equation 31 leads to the analytical expression for the first-order approximation of y,

$$y = \left(\frac{\kappa}{a}\right)^{\frac{1}{\kappa-1}} - \frac{\kappa + 1}{\kappa}. \tag{39}$$

3.3. Exact Solutions Versus Analytical Approximations

In Figure 1, we compare analytical approximations of zeroth order (dotted lines) and first order (solid lines) with the exact numerical solutions from Table 1 (orange squares), as obtained for different values of κ. The model parameters are set by assuming the exobase altitude at $r_0 = 6R_S$, a proton thermal speed of $w_{p0} = 182$ km/s (corresponding to $T_p = 10^6$ K), and an electron thermal speed of $w_{e0} = 5.5 \times 10^3$ km/s (corresponding to $T_e = 2 \times 10^6$ K). The results are limited to $\kappa > 3/2$, the validity range for the SKD, to keep the electron temperature physically meaningful. As κ approaches 3/2, the solution y in panel (a) becomes very large. The dotted line shows the approximate analytical solution of zeroth order Equation 29. Although this analytical estimate remains above unity for all κ, the condition $y_0 \gg 1$ is fulfilled only for $\kappa \lesssim 3$. Only in this low-κ range is the zeroth-order analytical approximation in good agreement with the exact numerical solution. The solid line represents the refined analytical solution, the first-order approximation in Equation 39, derived here for the first time and significantly improving the accuracy of the approximate solution for large κ.

Panel (b) of Figure 1 presents the ES potential at the exobase $\Phi_E(r_0)$, as a function of κ. The exact solutions (orange squares) are obtained from Equation 23 using the exact numerical evaluation of y in panel (a). The zeroth order approximation Equation 31 (dotted line) reproduces the exact solution only for $\kappa \lesssim 3$, while at higher values it increasingly overestimates $\Phi_E(r_0)$. The first-order analytical approximation (solid line) yields precise results for large values of κ. Panel (c) shows the terminal SW velocity $V_{\rm SW}$, obtained from Equation 5 using the values of $\Phi_E(r_0)$ from panel (b). The first order approximation (solid line), again, works well over a wide range of κ, in contrast to the zero order approximation, which systematically overestimates $V_{\rm SW}$ at larger κ. From this panel, it follows that, by assuming that electrons at the exobase follow a SKD distribution, the observed SW speeds ($\approx 300 - 800$ km/s) can be explained if their $\kappa \in (2.5, 7)$; the smaller the κ, the faster the wind. This property of SKD models has previously been outlined (e.g., Maksimovic, Pierrard, and Lemaire (1997)), and our results are consistent with these findings. We emphasize that the first-order analytical solution, derived in Section 3.2 for the first time, provides an accurate estimate for both the ES potential at the exobase and the corresponding terminal SW speed, as shown in Figure 1.

3.4. Radial Profiles

We now construct the radial profiles of the macro-parameters within the framework outlined in Section 2.2, using the boundary conditions at the exobase first provided by our exact (numerical) solutions. The same procedure can be performed with our approximate analytical expressions. The density profile has the general form given in Equation 7 and depends on the parameter C_0. Assuming Maxwellian protons at the exobase, as in Meyer-Vernet and Issautier (1998), the general definition of C_0, Equation 8, reduces to

$$C_0 = \frac{n_p(r_0)}{\sqrt{\pi}}\, P\left(\frac{V_{p0}}{w_{p0}}\right), \tag{40}$$

where

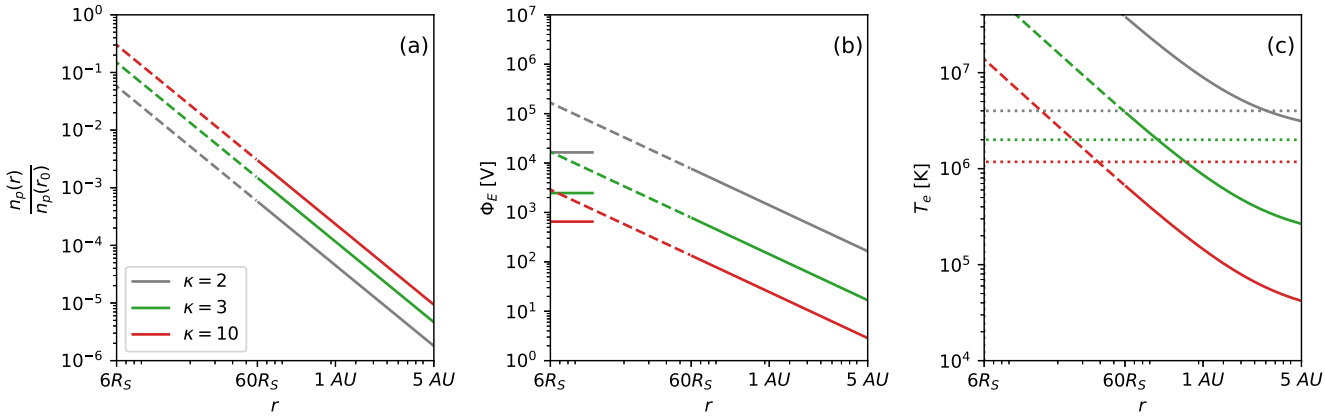

Figure 2. Radial profiles for (a) normalized density, (b) ES potential, and (c) electron temperature as a function of distance r (in units of R_S). The curves of different colors correspond to different values of the parameter $\kappa = 2, 3, 10$. Short lines in panel (b) indicate the ES potential at the exobase $\Phi_E(r_0)$ (boundary value at $r_0 = 6R_S$). The dotted lines in panel (c) mark the assumed electron temperatures at the exobase (see text).

$$\frac{P(x)}{\sqrt{\pi}} = \left(1/2 - x^2\right) e^{x^2} \left(1 - \mathrm{erf}(x)\right) + \frac{x}{\sqrt{\pi}}. \tag{41}$$

C_0 incorporates the influence of the ES and gravitational potentials through V_{p0}, defined in Equation 9. To evaluate V_{p0}, we use the exact solution for $\Phi_E(r_0)$ (orange markers in Figure 1b) and the gravitational potential $\Phi_G(r_0)$ defined in Equation 6. The exobase altitude is specified as $r_0 = 6R_S$.

The radial profile of the ES potential follows from the general Equation 10, which depends on the parameter D_0. Using the general definition of D_0 in Equation 11, where specified for SKD electrons, D_0 takes the form

$$D_0 = \frac{2 n_{e0} A_\kappa}{3(\kappa\, w_{e0}^2)^{3/2}} (1 + y)^{-\kappa - 1} \tag{42}$$

where

$$A_\kappa = \frac{\Gamma(\kappa + 1)}{\Gamma(\kappa - 1/2)\, \Gamma(3/2)}, \tag{43}$$

and

$$n_{e0} = \frac{n_e(r_0)}{1 - 12\, A_\kappa\, B_{x_0}(\kappa - 12, 32)}. \tag{44}$$

In Meyer-Vernet and Issautier (1998) n_{e0} is the normalization constant for the Kappa distribution, but here it is only a factor in expression Equation 42.

The radial profile of the electron temperature is obtained from the general Equations 12–14, which involve C_0, D_0, and B_2. C_0 and D_0 are given by Equations 38 and 42, respectively, while B_2 follows from the general definition Equation 15. For SKD electrons, it reduces to

$$B_2 = \frac{n_{e0}\, \kappa\, \theta_e^2}{2(2\kappa - 3)} (1 + y)^{-\kappa + \frac{1}{2}} \left(\kappa y + \frac{3}{2}\right), \tag{45}$$

where the exact solution y, obtained in Section 3.1, is substituted.

Radial profiles are shown in Figure 2. The gray, green and red curves correspond to $\kappa = 2, 3, 10$, respectively. Since the model equations are derived in the limit of large distances $\left(\eta \equiv (r_0/r)^2 \ll 1\right)$, we show the curves as solid lines only for $r/r_0 > 10$. The segments at low radial distances (down to the exobase altitude), where this assumption is not satisfied, are shown as dashed lines to indicate their limited reliability. Panel (a) displays the density, normalized by its value at $r = r_0$. All profiles follow a power law dependence with slope −2. For smaller κ, the density is lower, although all curves, by definition, converge to unity at $r = r_0$. This indicates that smaller κ values correspond to steeper density gradients at short distances, where the model itself is not valid. From the continuity equation in spherically symmetric flow, we find $V_r(r) = \text{const}/\left(r^2 n(r)\right)$, such that a smaller κ (lower n) implies faster acceleration, in accordance with previous results, for example, Maksimovic, Pierrard, and Lemaire (1997). Panel (b) of Figure 2 presents the radial profiles of $\Phi_E(r)$. The potential follows a universal power law and its magnitude is highly dependent on κ, when this parameter is small. Smaller κ values, which indicate a higher proportion of suprathermal electrons, result in a larger (more positive) Φ_E. Panel (c) shows the radial profiles of the electron temperature. At moderate but still large distances, temperature profiles decrease according to a power law, and then at larger distances they decrease asymptotically to a constant value. The temperatures at the exobase (dotted horizontal lines), $T_{\kappa 0} = \kappa/(\kappa - 3/2)T_{e0}$, increase with decreasing κ, compared to the Maxwellian limit (large κ) $T_{e0} = 10^6$ K. For small $\kappa = 2$ (gray lines), the temperature takes unrealistically high values that drop below the initial temperature only for vast distances.

4. RKD Electrons and Maxwellian Protons at the Exobase

We now assume that the electrons at the exobase have an RKD distribution

$$f_{e0} = C_{RKD}\left(1 + \frac{v^2}{\kappa w_{e0}^2}\right)^{-\kappa-1} \exp\left(-\frac{\alpha^2 v^2}{w_{e0}^2}\right). \tag{46}$$

The initial purpose of the cutoff parameter α was to ensure a consistent definition of all moments of the RKD model for any value of $\kappa > 0$ (Scherer et al., 2017). α can be determined from observations (Scherer et al., 2021), while the RKD model must reconcile two requirements: to reduce the non-physical effects of superluminal particles (with $v > c$, where c is the speed of light in a vacuum) in SKDs, and at the same time to preserve the effects of the measured suprathermal tail (Scherer, Fichtner, et al., 2019). As a result, this parameter must roughly satisfy $w_{e0}/c < \alpha < 1$, a condition that we will also take into account below when choosing values for α (for our $w_{e0} = 5.5 \times 10^3$ km/s, then α must satisfy $0.018 < \alpha < 1$).

The normalization constant C_{RKD} is determined using Equation 3, where the second integral on the right side is neglected in the limit of large $V_> > w_{e0}$ (Meyer-Vernet & Issautier, 1998)

$$C_{RKD} = \frac{n_e(r_0)}{(\pi w_{e0}^2 \kappa)^{3/2} U(3/2, 3/2 - \kappa, \alpha^2 \kappa)}, \tag{47}$$

where U is the hypergeometric Kummer (or Tricomi) function (Abramowitz & Stegun, 1965). For the electron flux in Equation 1, we obtain

$$F_e = \frac{\kappa^2 w_{e0}^4}{2} C_{RKD} \exp(-\beta y) \times \left[\beta^{\kappa-1} U(\kappa, \kappa, \beta(1+y)) - \beta^{\kappa} U(1+\kappa, 1+\kappa, \beta(1+y))\right], \tag{48}$$

where $\beta = \alpha^2\kappa$, and $y = V_0^2/(\kappa w_{e0})$ is the same as above in Equation 22. For Maxwellian protons, their flux on the right side of Equation 1 reads then explicitly as

$$F_p = \frac{n_p(r_0)\, w_{p0}}{\pi^{3/2}}. \tag{49}$$

4.1. Exact Solutions

Substituting Equations 48 and 49 into Equation 1, and taking into account $n_e(r_0) = n_p(r_0)$, we find

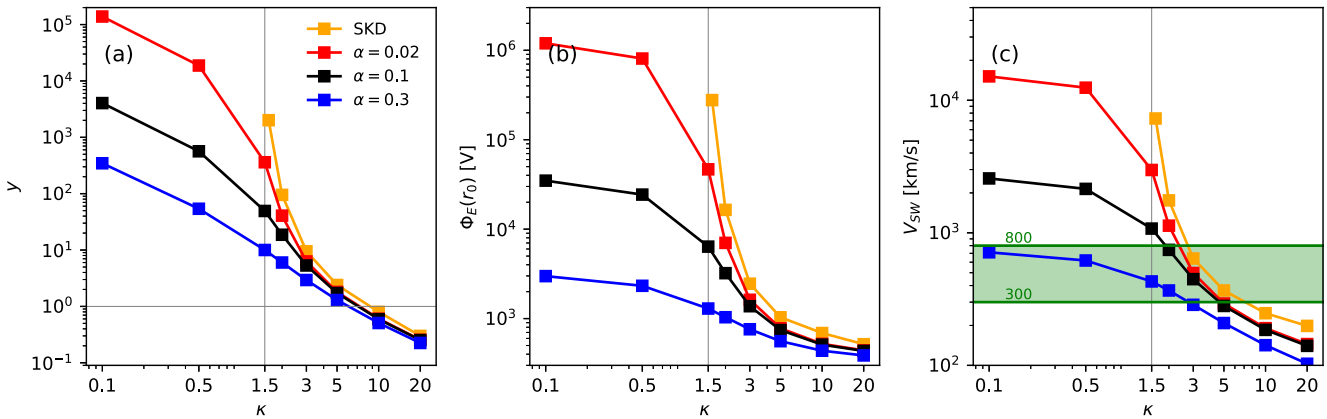

Figure 3. The dependence of the (exact) solutions at the exobase on κ for RKD electrons, in the same format as Figure 1. Results are plotted for three cutoffs $\alpha = 0.02$ (red), $\alpha = 0.1$ (black) and $\alpha = 0.3$ (blue), and are compared with the results for SKD electrons (orange) from Figure 1. The greenish range in panel (c) indicates observed SW speeds (300–800 km/s).

$$\frac{w_{p0}}{w_{e0}} = \frac{\sqrt{\kappa} e^{-\beta y}}{2U(3/2, 3/2-\kappa, \beta)}\left[\beta^{\kappa-1} U(\kappa, \kappa, \beta(1+y)) - \beta^{\kappa} U(1+\kappa, 1+\kappa, \beta(1+y))\right]. \tag{50}$$

This equation is solved with Brent's root finding method (Brent, 1973), for the same thermal speeds at the exobase ($r_0 = 6\ R_S$) $w_{p0} = 182$, and $w_{e0} = 5.5 \times 10^3$ km/s, corresponding to $T_{p0} = m_p w_{p0}^2/2k_B = 2 \times 10^6$ and $T_{e0} = m_e w_{e0}^2/2k_B = 10^6$ K. Note that for RKD electrons, the physical temperature is a function of α and κ (Scherer, Lazar, et al., 2019)

$$T_{r\kappa} = T_{e0}\ \kappa\ U\big(5/2, 5/2-\kappa, \alpha^2\kappa\big)/U\big(3/2, 3/2-\kappa, \alpha^2\kappa\big). \tag{51}$$

We have also examined the possibility of deriving an approximate analytical solution of Equation 50. However, with the numerical solution for y we found that the argument of the U-function, $z = \beta(1 + y)$, remains close to unity. As a result, the U-function could not be expanded in a useful manner, preventing the derivation of an approximate analytical solution.

The exact solutions for y are presented in Figure 3, panel (a), with the blue, black, and red curves corresponding to the RKD electrons with different values of the cutoff parameter α. For comparison, the orange curve shows the exact solution of Equation 24 for SKD electrons. As the cutoff parameter α decreases to 0, the RKD reduces to the SKD, and the RKD solutions become closer to those for SKD electrons. Panel (b) of Figure 3 shows the ES potential at the exobase $\Phi_E(r_0)$, derived from y in panel (a), using Equation 23. Panel (c) of Figure 3 represents the SW terminal velocity V_{SW} obtained from Equation 5, using $\Phi_E(r_0)$ from panel (b). At large κ, the $y(\kappa)$ curves for RKD electrons with different α converge very closely. However, the corresponding curves obtained for $\Phi_E(r_0)$ and V_{SW} are still slightly separated; see the slight difference between the red (RKD solution for lowest (still finite) $\alpha = 0.02$) and orange curves. This is mainly because the relationship between y and Φ_E involves a scaling factor, linearly dependent on κ, which amplifies even minor differences when κ increases. In addition, the derivation of Equation 13 for SKD accounts for both integrals in Equation 3, without assuming that V_0 is much larger than the most probable speed of the electron distribution. In contrast, the RKD derivation of Equation 50 relies on the approximation that V_0 is much larger than the most probable electron speed, allowing the second integral in Equation 3 to be neglected. This simplification likely accounts for the remaining mismatch.

The most important feature of the model with RKD electrons at the exobase is the possibility of investigating extended conditions, including the low-$\kappa \leqslant 3/2$ regimes. The applicability of SKD is limited to $\kappa > 3/2$. We find that for RKD electrons, $\Phi_E(r_0)$ and the resulting V_{SW} approach finite values as $\kappa \to 0$, with the saturation level controlled by α. For SKD electrons, reproducing the observed SW speed (green band) requires $3 < \kappa < 7$. In contrast, RKD electron models can predict, depending on the values of the parameter α, a bulk velocity V_{SW} in the observationally relevant range even for very small κ, below the critical value for SKD, $\kappa \leqslant 3/2$.

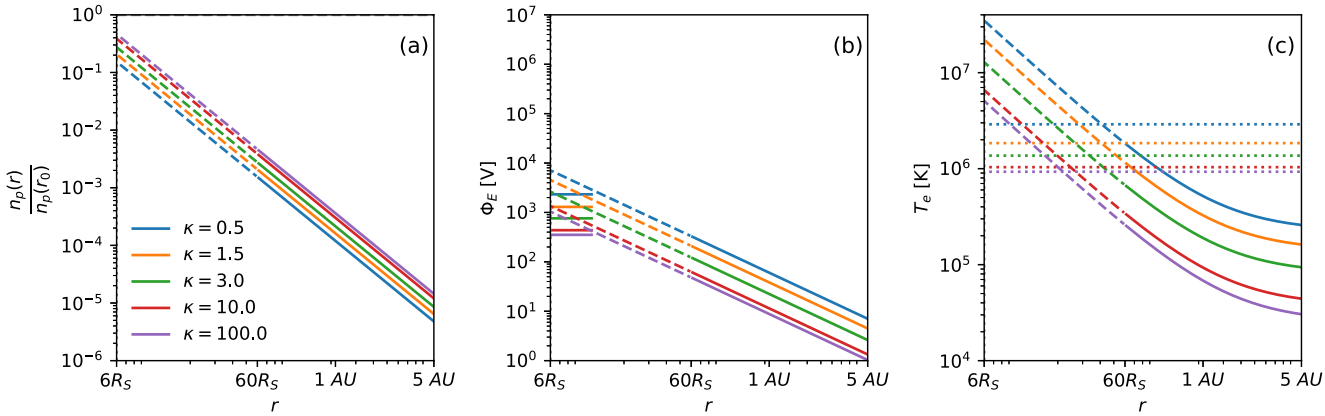

Figure 4. Radial profiles for (a) normalized density, (b) ES potential and (c) electron temperature for RKD electrons with $\alpha = 0.3$ and different values of κ. Short lines in panel (b) indicate $\Phi_E(r_0)$ (boundary values) at the exobase $r_0 = 6R_S$). The dotted lines in panel (c) mark the assumed electron temperatures at the exobase (see text).

4.2. Radial Profiles

We now investigate how regularization of the suprathermal distribution tails (quantified by the parameter α) modifies the radial profiles compared to the SKD model. We keep the assumption that protons follow a Maxwellian distribution, as in Section 3. In the general expression Equation 7 for the radial density profile, we now use C_0 given by Equations 40 and 41. The difference arises in the evaluation of V_{p0} from Equation 9: instead of using the ES potential at the exobase derived for SKD electrons, we now adopt $\Phi_E(r_0)$, shown in Figure 3b and obtained for RKD electrons. The radial profile of the ES potential is determined by the general Equation 10, which involves two parameters C_0, as explained above, and D_0. The parameter representing the contribution of the non-escaping electrons, D_0, is evaluated using Equation 11, where f_{e0} is the RKD electron distribution function defined in Equation 46. To build the radial profile of the electron temperature, we use the general Equations 12–14. Parameters C_0 and D_0 are calculated as explained above, while B_2 is given by

$$B_2 = \pi \int_{V_0}^{\infty} dv v^3 \sqrt{v^2 - V_0^2} f_{e0}(v), \tag{52}$$

and is evaluated numerically. Physically, the product $B_2\eta$ represents the contribution of escaping electrons to the second-order velocity moment, that is, their role in determining the temperature profile.

Figure 4 shows the resulting radial profiles for RKD electrons with a strong cut-off parameter $\alpha = 0.3$ and different values of κ. Radial profiles are obtained in the limit of large distances from the Sun $\left(\eta = r_0^2/r_2 \ll 1\right)$. As in Figure 2, the profiles are shown as solid lines for $r > 60R_S$, where this assumption is valid, and with dashed lines for lower distances. Panel (a) of Figure 4 shows the density profiles normalized to their value at r_0. The density is lower for smaller κ. This trend is the same as in the case of SKD electrons, shown in Figure 2a. However, in contrast to the case with SKD electrons, the densities for different κ are much closer. Again, by the definition of normalization, all profiles should converge to 1 at $r = r_0$. Thus, the density gradient at short distances (where the model is not valid) is smaller in the model with RKD electrons, and the SW acceleration is reduced. The reason is that $\alpha = 0.3$ imposes a strong cut-off that significantly suppresses the suprathermal distribution tails. Panel (b) of Figure 4 shows the radial profiles of the ES potential. Φ_E increases, as expected if suprathermal electron tails become heavier (smaller κ). In contrast to the case with SKD, shown in Figure 2b, $\Phi_E(r)$ increases only slightly as κ decreases. The reason for this effect is that the cut-off parameter reduces the unrealistic part of the tails of the SKD electron distribution. Panel (c) of Figure 4 shows the radial profiles of the electron temperature, with dotted lines marking the initial RKD electron temperatures given by Equation 51; see also Table 2 for the temperature ratios obtained for different values of α and κ. The overall trend resembles that of the SKD case in Figure 2c: smaller values of κ correspond to higher T_e. However, unlike SKD, the RDK with $\alpha = 0.3$ predicts lower temperatures, even for small κ, which may provide more realistic descriptions.

Table 2
Temperature Ratios T_{rk}/T_{e0} Relating Maxwellian Temperature ($T_{e0} = 10^6$ K) to RKD Temperature T_{rk} Defined by Equation 51, for Various Values of α and κ

α	κ	T_{rk}/T_{e0}
0.02	0.5	226.89
0.02	1.5	8.41
0.02	3.0	1.99
0.02	10.0	1.18
0.02	100.0	1.01
0.3	0.5	2.90
0.3	1.5	1.84
0.3	3.0	1.37
0.3	10.0	1.04
0.3	100.0	0.93

Figure 5 shows the radial profiles for RKD electrons with a much smaller cut-off parameter $\alpha = 0.02$. In this limit, the profiles are more similar to those obtained for SKD electrons, as shown in Figure 2. However, the RKD formulation also allows exploration of $\kappa \leqslant 3/2$, corresponding to even heavier-tailed distributions and not accessible in the SKD model. In particular, for these new cases, the relative density shown in panel (a) drops to very low levels at large distances, implying a stronger SW acceleration. As an immediate consequence, in panel (b), the ES potential reaches higher values. Also, the temperature shown in panel (c) increases to higher values (e.g., for $\kappa < 3$), which are unrealistic for the SW, but can eventually describe stellar winds of stars with much hotter coronas (Güdel, 2004). The contrasting results obtained in Figures 4 and 5 demonstrate the important role of the regularization parameter $\alpha < 1$. Despite the complexity of the new RKD models, they can describe a more pronounced presence of suprathermal electrons even in the solar corona and a consistent contribution to the acceleration of SW streams, without overestimating the acceleration due to unphysical (superluminal) populations. It is also very plausible that excessive suprathermal electrons with $\kappa \leqslant 3/2$ can be found in plasma sources of energetic events, such as coronal eruptions and coronal mass ejections (CMEs). If future in situ observations, or at least remote spectral analyses (Dudík & Dzifčáková, 2021; Effenberger & Jeffrey, 2021), adapt RKDs and highlight energetic electrons at the exobase, then exospheric models could explain CME-like outflows with speeds of up to several thousand km/s.

5. Conclusions

Recent advances in both observations of suprathermal electrons in the solar corona and consistent modeling of these suprathermal populations using RKDs give new impetus to macroscopic modeling of the SW based on the kinetic properties of its components, electrons and protons. RKDs are adjustments to SKDs to address the latter's inconsistencies (see details in the introduction). In this paper, we have exploited the method proposed by Meyer-Vernet and Issautier (1998) for the semi-analytical derivation of key parameters at the exobase, such as the ES potential, as well as the properties of the SW, for example, density, electron temperature, and their variation with heliocentric distance (radial profiles). First, we have refined the previous model based on SKD electrons at the exobase, for which we derived rigorous, fully analytical approximations. These facilitate not only numerical calculations in the development of exospheric models but also comparison with the new estimates based on the presence of RKD electrons at the exobase.

New models with RKD electrons can prevent overestimating SW properties at large distances, including energies, temperatures, and bulk speeds. Recent PSP observations (Abraham et al., 2022; Zheng et al., 2024) reveal an

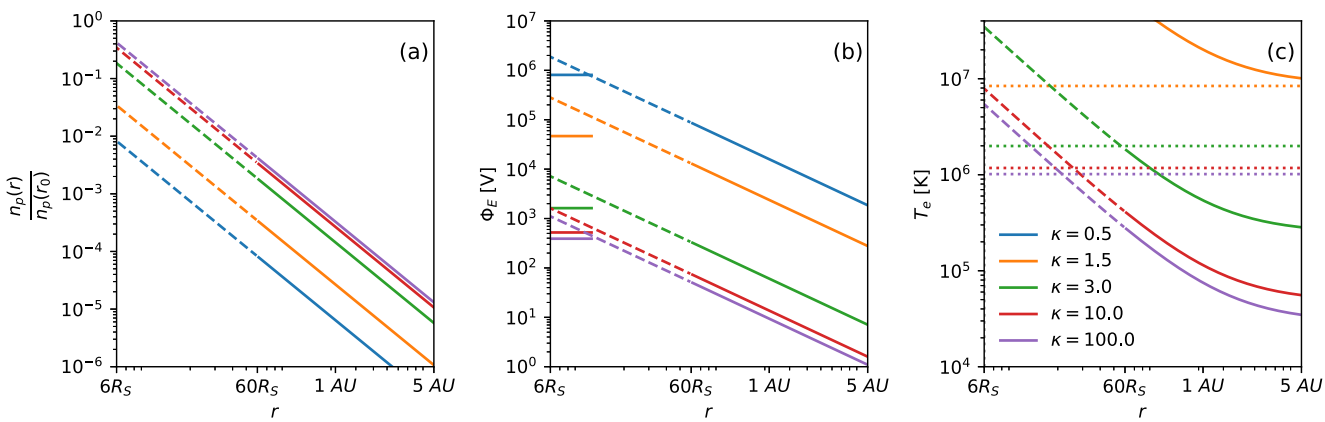

Figure 5. Radial profiles of (a) normalized density, (b) ES potential and (c) electron temperature for the model with RKD electrons with $\alpha = 0.02$ and different values of κ. Short lines in panel (b) indicate $\Phi_E(r_0)$ (boundary values) at the exobase $r_0 = 6R_S$). The dotted lines in panel (c) mark the assumed electron temperatures at the exobase (see text).

increased abundance of suprathermal electrons at the exobase associated with reduced κ parameters, for example, $\kappa \to 4$ (and perhaps even less, according to the decreasing trend), for which SKD modeling generally leads to such overestimations. The advantage of RKD models is that the suprathermal influence can be weighted by adjusting the new cutoff parameter $\alpha < 1$. Thus, estimates of the temperatures and bulk speeds of the SW can remain realistic, depending on the value of α, and be of the order of those reported by observations. In this case, the new parameterizations are still at a semi-analytical level, due to their complexity, being expressed in terms of Tricomi hypergeometric integral functions that do not allow for physically meaningful approximations. Instead, an extensive and consistent characterization is offered for various initial (or boundary) conditions at the exobase. Electron VDs with strong suprathermal tails described by low $\kappa \leqslant 3/2$, that is, below the critical threshold for SKDs, can also be considered. These can be associated, as a plausible hypothesis (still to be confirmed by the observations), with events much more energetic than the SW, such as coronal flares and CMEs. In addition, such conditions cannot be excluded as being conducive to the modeling of stellar winds in the astrospheres of stars with much hotter coronas, with temperatures up to two orders of magnitude higher than that of the solar corona (Güdel, 2004).

Appendix A: Moments for Protons

In the limit of large distances, the proton moments of order q can be approximated as (Meyer-Vernet & Issautier, 1998)

$$M_{pq} \approx C_q \eta, \tag{A1}$$

where

$$C_q = \pi \int_0^\infty dv \frac{v^3}{\left(v^2 + V_{p0}^2\right)^{(1-q)/2}} f_{p0}(v), \tag{A2}$$

V_{p0} is defined by Equation 9, and f_{p0} is the proton distribution function at the exobase. The derivation uses conservation of energy and magnetic moment, along with Liouville's theorem. The phase-space limits are simplified to calculate the moments, assuming large distances from the Sun.

Appendix B: Moments for Electrons

In the limit of large distances, the moment of order q of the electron distribution can be approximated as follows (Meyer-Vernet & Issautier, 1998)

$$M_{eq} \approx D_q v_M^{q+3} + B_q \eta, \tag{B1}$$

where

$$D_q = 4\pi f_{e0}(V_0)/(q+3), \tag{B2}$$

and

$$B_q = \pi \int_{V_0}^\infty dv v^3 \left(v^2 - V_0^2\right)^{(q-1)/2} f_{e0}(v). \tag{B3}$$

The first and second terms in Equation B1 correspond to nonescaping and escaping electrons, respectively.

Appendix C: Equivalence of Normalizations

Here we demonstrate that the SKD normalization used in Meyer-Vernet and Issautier (1998) is equivalent to that used in Section 3. Meyer-Vernet defines the distribution with a generic constant n_{e0}, which is related to the

physical density at the exobase $n_e(r_0)$ through their Equation 63. This relation involves the function $\beta_2(y)$ defined in their Equation 64. In contrast, our formulation, given in Equation 19 uses the incomplete beta function $B_{x_0}(3/2, \kappa - 1/2)$ with $x_0 = y/(1 + y)$. The link between these two forms follows from the *symmetry relation* for the incomplete beta function (Abramowitz & Stegun, 1965, Equation 6.6.3)

$$B_x(a,b) + B_{1-x}(b,a) = B(a,b). \tag{C1}$$

Applying this identity with $z = 1/(1 + y)$ yields

$$B_{x_0}\left(\frac{3}{2}, \kappa - \frac{1}{2}\right) = \frac{1 - \beta_2(z)}{A_\kappa}, \tag{C2}$$

where A_κ is given in Equation 43.

Conflict of Interest

The authors declare no conflicts of interest relevant to this study.

Data Availability Statement

The Jupyter Notebooks to execute the analysis in the paper can be found at https://github.com/ISashaVinogradov/kappa-electrons-solar-wind, is hosted at GitHub, and is preserved at Zenodo (Vinogradov, 2026) (Version JGR2025_v1.0, https://doi.org/10.5281/zenodo.18152868). Solutions were obtained using Brent's method (brentq) from the publicly available SciPy library. We also used mpmath (BSD license) to evaluate special functions with arbitrary precision, and NumPy for numerical array operations. The plots were generated using Matplotlib, which is distributed under the Matplotlib (PSF) license available at https://matplotlib.org/.

Acknowledgments
The authors acknowledge support from the Ruhr-University Bochum and the Katholieke Universiteit Leuven. These results were also obtained in the framework of the projects C16/24/010 (C1 project Internal Funds KU Leuven), G0B5823N (FWO-Vlaanderen), WEAVE project G002523N/FI 706/31-1 (FWO-Vlaanderen/DFG-Germany), and 4000134474 (SIDC Data Exploitation, ESA Prodex). Powered@NLHPC: This research was partially supported by the supercomputing infrastructure of the NLHPC (CCSS210001). The resources and services used in this work were provided by the VSC (Flemish Supercomputer Center), funded by the Research Foundation—Flanders (FWO) and the Flemish Government. SP is funded by the European Union (ERC, Open SESAME, 101141362). VP thanks the Solar-Terrestrial Center of Excellence for its support. Views and opinions expressed are, however, those of the author(s) only and do not necessarily reflect those of the European Union or the European Research Council. Neither the European Union nor the granting authority can be held responsible for them.

References

Abraham, J. B., Owen, C. J., Verscharen, D., Bakrania, M., Stansby, D., Wicks, R. T., et al. (2022). Radial evolution of thermal and suprathermal electron populations in the slow solar wind from 0.13 to 0.5 au: Parker solar probe observations. *The Astrophysical Journal*, *931*(2), 118. https://doi.org/10.3847/1538-4357/ac6605

Abramowitz, M., & Stegun, I. A. (1965). Handbook of mathematical functions with formulas, graphs, and mathematical tables.

Brent, R. P. (1973). *Algorithms for minimization without derivatives* (1st ed.). Prentice-Hall.

Dudík, J., & Dzifčáková, E. (2021). Diagnostics of Kappa distributions from optically thin solar spectra. In M. Lazar & H. Fichtner (Eds.), *Kappa distributions; from observational evidences via controversial predictions to a consistent theory of nonequilibrium plasmas* (Vol. 464, pp. 53–87). https://doi.org/10.1007/978-3-030-82623-9_4

Effenberger, F., & Jeffrey, N. L. S. (2021). Non-thermal and Kappa distributions in solar flare radiative signatures. In M. Lazar & H. Fichtner (Eds.), *Kappa distributions; from observational evidences via controversial predictions to a consistent theory of nonequilibrium plasmas* (Vol. 464, pp. 89–103). https://doi.org/10.1007/978-3-030-82623-9_5

Feldman, W. C., Asbridge, J. R., Bame, S. J., Montgomery, M. D., & Gary, S. P. (1975). Solar wind electrons. *Journal of Geophysical Research*, *80*(31), 4181–4196. https://doi.org/10.1029/JA080i031p04181

Güdel, M. (2004). X-ray astronomy of stellar coronae. *Astronomy and Astrophysics Review*, *12*(2–3), 71–237. https://doi.org/10.1007/s00159-004-0023-2

Husidic, E., Scherer, K., Lazar, M., Fichtner, H., & Poedts, S. (2022). Toward a realistic evaluation of transport coefficients in non-equilibrium space plasmas. *The Astrophysical Journal*, *927*(2), 159. https://doi.org/10.3847/1538-4357/ac4af4

Lamy, H., Pierrard, V., Maksimovic, M., & Lemaire, J. F. (2003). A kinetic exospheric model of the solar wind with a nonmonotonic potential energy for the protons. *Journal of Geophysical Research*, *108*(A1). https://doi.org/10.1029/2002JA009487

Lazar, M. & Fichtner, H. (Eds.) (2021)., *Kappa distributions; from observational evidences via controversial predictions to a consistent theory of nonequilibrium plasmas* (Vol. 464). https://doi.org/10.1007/978-3-030-82623-9

Lazar, M., Pierrard, V., Poedts, S., & Fichtner, H. (2020). Characteristics of solar wind suprathermal halo electrons. *Astronomy & Astrophysics*, *642*, A130. https://doi.org/10.1051/0004-6361/202038830

Lazar, M., Scherer, K., Fichtner, H., & Pierrard, V. (2020). Toward a realistic macroscopic parametrization of space plasmas with regularized κ-distributions. *Astronomy and Astrophysics*, *634*, A20. https://doi.org/10.1051/0004-6361/201936861

Lemaire, J., & Scherer, M. (1971). Simple model for an ion-exosphere in an open magnetic field. *The Physics of Fluids*, *14*(8), 1683–1694. https://doi.org/10.1063/1.1693664

Lomazzi, P., Rouillard, A. P., Lavarra, M. A., Poirier, N., Blelly, P.-L., Dakeyo, J.-B., et al. (2025). A parametric study of solar wind properties and composition using fluid and kinetic solar wind models. *The Astrophysical Journal*, *984*(2), 198. https://doi.org/10.3847/1538-4357/adc2f6

Maksimovic, M., Pierrard, V., & Lemaire, J. F. (1997a). A kinetic model of the solar wind with Kappa distribution functions in the Corona. *A&A*, *324*, 725–734.

Maksimovic, M., Pierrard, V., & Riley, P. (1997). Ulysses electron distributions fitted with Kappa functions. *Geophysical Research Letters*, *24*(9), 1151–1154. https://doi.org/10.1029/97GL00992

Meyer-Vernet, N., & Issautier, K. (1998). Electron temperature in the solar wind: Generic radial variation from kinetic collisionless models. *Journal of Geophysical Research*, *103*(A12), 29705–29718. https://doi.org/10.1029/98JA02853

Osuna Alcalaya, P., Zouganelis, I., & Rodríguez Pacheco, J. (2021). Analytic solution for the electrostatic potential of the solar wind. *A&A*, *653*, A75. https://doi.org/10.1051/0004-6361/202040047

Péters de Bonhome, M., Pierrard, V., & Bacchini, F. (2025). A kinetic model of solar wind acceleration driven by Ambipolar electric potential and velocity-space diffusion. *A&A*, *697*, A104. https://doi.org/10.1051/0004-6361/202554250

Pierrard, V., & Lazar, M. (2010). Kappa distributions: Theory and applications in space plasmas. *Solar Physics*, *267*(1), 153–174. https://doi.org/10.1007/s11207-010-9640-2

Pierrard, V., Lazar, M., & Schlickeiser, R. (2011). Evolution of the electron distribution function in the whistler wave turbulence of the solar wind. *Solar Physics*, *269*(2), 421–438. https://doi.org/10.1007/s11207-010-9700-7

Pierrard, V., Maksimovic, M., & Lemaire, J. (2001). Self-consistent model of solar wind electrons. *Journal of Geophysical Research*, *106*(A12), 29305–29312. https://doi.org/10.1029/2001JA900133

Pierrard, V., Péters de Bonhome, M., Halekas, J., Audoor, C., Whittlesey, P., & Livi, R. (2023). Exospheric solar wind model based on regularized kappa distributions for the electrons constrained by parker solar probe observations. *Plasma*, *6*(3), 7518–7540. https://doi.org/10.3390/plasma6030036

Scherer, K., Fichtner, H., Fahr, H. J., & Lazar, M. (2019). On the applicability of κ-distributions. *The Astrophysical Journal*, *881*(2), 93. https://doi.org/10.3847/1538-4357/ab2df9

Scherer, K., Fichtner, H., & Lazar, M. (2017). Regularized κ-distributions with non-diverging moments. *EPL (Europhysics Letters)*, *120*(5), 50002. https://doi.org/10.1209/0295-5075/120/50002

Scherer, K., Husidic, E., Lazar, M., & Fichtner, H. (2021). Generalized anisotropic κ-cookbook: 2D fitting of Ulysses electron data. *Monthly Notices of the Royal Astronomical Society*, *501*(1), 606–613. https://doi.org/10.1093/mnras/staa3641

Scherer, K., Lazar, M., Husidic, E., & Fichtner, H. (2019). Moments of the anisotropic regularized κ-distributions. *The Astrophysical Journal*, *880*(2), 118. https://doi.org/10.3847/1538-4357/ab1ea1

Shen, C., Li, X., Ko, Y.-K., Raymond, J. C., Guo, F., Polito, V., & Pierrard, V. (2025). Modeling of ionization and recombination processes in plasma with arbitrary non-Maxwellian electron distribution. *The Astrophysical Journal*, *988*(2), 151. https://doi.org/10.3847/1538-4357/ade2cf

Štverák, Š., Trávníček, P., Maksimovic, M., Marsch, E., Fazakerley, A. N., & Scime, E. E. (2008). Electron temperature anisotropy constraints in the solar wind. *Journal of Geophysical Research: Space Physics*, *113*(A3). https://doi.org/10.1029/2007JA012733

Vinogradov, A. (2026). Isashavinogradov/kappa-electrons-solar-wind: Paper-version. *Zenodo*. https://doi.org/10.5281/zenodo.18152868

Vocks, C., Salem, C., Lin, R. P., & Mann, G. (2005). Electron Halo and Strahl formation in the solar wind by resonant interaction with whistler waves. *The Astrophysical Journal*, *627*(1), 540–549. https://doi.org/10.1086/430119

Wilson, L. B., Chen, L.-J., Wang, S., Schwartz, S. J., Turner, D. L., Stevens, M. L., et al. (2019). Electron energy partition across interplanetary shocks. II. Statistics. *The Astrophysical Journal Supplement Series*, *245*(2), 24. https://doi.org/10.3847/1538-4365/ab5445

Zheng, X., Martinović, M. M., Pierrard, V., Klein, K. G., Liu, M., Abraham, J. B., et al. (2024). Radial evolution of non-Maxwellian electron populations derived from quasi-thermal noise spectroscopy: Parker solar probe observations. *The Astrophysical Journal*, *977*(1), 39. https://doi.org/10.3847/1538-4357/ad7d05

Zouganelis, I., Maksimovic, M., Meyer-Vernet, N., Lamy, H., & Issautier, K. (2004). A transonic collisionless model of the solar wind. *The Astrophysical Journal*, *606*(1), 542–554. https://doi.org/10.1086/382866